

# Confocal FRET Microscopy to Measure Clustering of Ligand-Receptor Complexes in Endocytic Membranes

Horst Wallrabe,\* Masilamani Elangovan,<sup>†</sup> Almut Burchard,<sup>‡</sup> Ammasi Periasamy,<sup>\*†</sup> and Margarida Barroso\*

\*Department of Biology, <sup>†</sup>W. M. Keck Center for Cellular Imaging, and <sup>‡</sup>Department of Mathematics, University of Virginia, Charlottesville, Virginia 22904 USA

**ABSTRACT** The dynamics of protein distribution in endocytic membranes are relevant for many cellular processes, such as protein sorting, organelle and membrane microdomain biogenesis, protein-protein interactions, receptor function, and signal transduction. We have developed an assay based on Fluorescence Resonance Energy Microscopy (FRET) and novel mathematical models to differentiate between clustered and random distributions of fluorophore-bound molecules on the basis of the dependence of FRET intensity on donor and acceptor concentrations. The models are tailored to extended clusters, which may be tightly packed, and account for geometric exclusion effects between membrane-bound proteins. Two main criteria are used to show that labeled polymeric IgA-ligand-receptor complexes are organized in clusters within apical endocytic membranes of polarized MDCK cells: 1), energy transfer efficiency ( $E\%$ ) levels are independent of acceptor levels; and 2), with increasing unquenched donor: acceptor ratio,  $E\%$  decreases. A quantitative analysis of cluster density indicates that a donor-labeled ligand-receptor complex should have 2.5–3 labeled complexes in its immediate neighborhood and that clustering may occur at a limited number of discrete membrane locations and/or require a specific protein that can be saturated. Here, we present a new sensitive FRET-based method to quantify the co-localization and distribution of ligand-receptor complexes in apical endocytic membranes of polarized cells.

## INTRODUCTION

To understand cellular processes such as protein sorting, organelle and membrane microdomain biogenesis, protein-protein interactions, receptor function and signal transduction, it is important to know which specific cellular components are distributed in close proximity within the membrane. We are proposing that a clustering process occurs during the sorting of ligand-receptor complexes in endocytic trafficking in polarized cells. In particular, we have examined whether complexes between polymeric IgA receptor (pIgA-R) and its ligands organize in a clustered manner in the apical endocytic compartments of polarized MDCK cells.

Polarized epithelial cells have two distinct plasma membranes (PMs), apical and basolateral PMs, separated by tight junctions. Proteins are transported between these two PM domains via the transcytotic pathway, which is facilitated by a network of membrane-bound compartments that are partially shared with other endocytic pathways (Fig. 1). Polarized epithelial MDCK cells stably transfected with pIgA-R are one of the best-studied transcytotic models. Still, questions concerning the morphology, organization, and regulation of the endocytic compartments involved in the transcytotic pathway remain open.

Several lines of evidence indicate that the apical endocytic compartments of polarized epithelial MDCK cells, including the apical early endosome (AEE), the apical recycling endosome (ARE), and to lesser extent, the common endosome (CE), are excellent models to study endosomal protein

sorting (Barroso and Sztul, 1994; Apodaca et al., 1994; Brown et al., 2000; Gibson et al., 1998). First, they are clearly compartmentalized into vacuolar areas containing fluid-phase components (AEE) and tubulo-vesicular structures (AEE and ARE) containing only membrane-bound cargo (Barroso and Sztul, 1994; Leung et al., 2000). Second, they can be imaged by following the trafficking of pIgA-R, a well-known marker for basolateral-to-apical transcytosis and apical recycling, and by their proximal localization to the apical PM (Apodaca et al., 1994; Barroso and Sztul, 1994). Third, trafficking through apical endocytic compartments is regulated by signaling molecules, providing an additional level of molecular control to the apical targeting pathway (Hansen and Casanova, 1994; Huttner and Zimmerberg, 2001; Van Ijzendoorn et al., 2000; Winckler and Mellman, 1999).

For our quantitative analysis of receptor clustering in the apical endocytic compartments, we used laser scanning confocal microscopy and fluorescence resonance energy transfer (FRET), in particular, the parameter of energy transfer efficiency ( $E\%$ ) (Wu and Brand, 1994; Periasamy and Day, 1999; Day et al., 2001; Kenworthy, 2001). As a first step we have internalized pIgA-R ligands—labeled with different fluorophores (*donor* and *acceptor*)—from opposite PMs in MDCK cells at 17°C, which blocks delivery from the apical endocytic compartments to the apical PM (Hunziker et al., 1990; Barroso and Sztul, 1994). On binding, the basolaterally internalized pIgA-R-ligand complexes are transported to the apical PM (Fig. 1, *arrows 1, 4, 6–7*), whereas the apically internalized ligand-receptor complexes are endocytosed from the apical PM and recycled back to the apical PM (Fig. 1, *arrows 6–11*). Basolaterally and apically internalized pIgA-R-ligand complexes will eventually co-localize and accumulate in apical endocytic compartments,

Submitted April 16, 2002, and accepted for publication March 17, 2003.

Address reprint requests to Margarida Barroso, Tel.: 434-243-7616; Fax: 434-982-5626; E-mail: mmb8n@virginia.edu.

© 2003 by the Biophysical Society

0006-3495/03/07/559/13 \$2.00

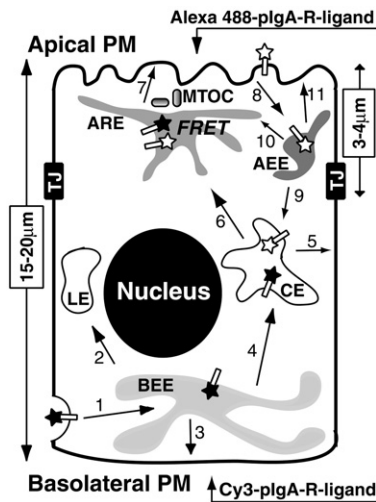


**FIGURE 1** Endocytic trafficking pathways in polarized epithelial MDCK cells and subapical co-localization of differently labeled pIgA-R ligands internalized from opposite PMs. Different membrane trafficking pathways exist—partially shared—for different internalized components. The basolateral-to-apical transcytotic pathway (arrows 1, 4, and 6–7) and the apical receptor recycling pathway (arrows 6–11) are used by basolaterally and apically internalized pIgA-R-ligand complexes, respectively. Arrows 1–3 and 1, 4, and 5 show pathways for basolateral receptor recycling, which can also be used by basolaterally internalized pIgA-R-ligand complexes. Arrows 1–2 show the basolateral PM to lysosomal pathway. The pIgA-R-ligand complexes accumulate in apical endocytic compartments (e.g., ARE, AEE, and at a lesser extent, CE) upon internalization at 17°C by blocking delivery to the apical PM (Hunziker et al., 1990; Barroso and Sztul, 1994). The solid star represents the basolaterally internalized Cy3-pIgA-R-ligand complex (Acceptor). The open star is the apically internalized Alexa 488-pIgA-R-ligand complex (Donor). In this example, both complexes first cross in the CE and then co-localize and accumulate in the ARE, where FRET may occur (Barroso and Sztul, 1994). AEE, apical early endosome; BEE, basolateral early endosome; ARE, apical recycling compartment; CE, common endosome; and LE, late endosome.

just below the apical PM (Fig. 1 shows an example of co-localization in the ARE; see Barroso and Sztul, 1994; Apodaca et al., 1994). It is the purpose of our experiments to use FRET microscopy to determine whether clustering precedes their forward transport from apical endocytic compartments to the apical PM.

FRET occurs when donor and acceptor fluorophores have sufficiently large spectral overlap, favorable dipole-dipole orientation, proximity of 1–10 nm, and large enough quantum yield (Lakowicz, 1999). The very spectral overlap, however, is the cause of significant FRET contamination due to overlapping donor and acceptor emission spectra (donor cross-talk) and that part of the acceptor absorption spectrum which is excited by the donor wavelength (acceptor bleed-through). Several methods have been developed to correct the contamination, each with certain limitations depending on the level of sensitivity desired (Bastiaens and Jovin, 1996; Gordon et al., 1998; Wouters et al., 1998; Chamberlain et al., 2000; Xia and Liu, 2001; Zal et al., 2002). In our biological system, fluorophore pairs are not separated by a consistent

distance and FRET occurs over a wide range of fluorescence intensities at a membrane plane, and thus it is essential to use a FRET assay with a highly sensitive contamination correction system. We have used an algorithm-based method to correct the spillover contamination in a pixel-by-pixel manner, which is favorable to obtain highly sensitive corrected FRET signals (Elangovan et al., 2003).

The relationship between  $E\%$  and acceptor and unquenched donor ( $uD$ ) levels was used to determine that differently labeled ligand-receptor complexes are distributed in a clustered manner in apical endocytic membranes. As modeled previously, independence of  $E\%$  from acceptor levels is one indicator of a clustered assembly (Kenworthy and Edidin, 1998). Another indicator demonstrated in this article is the decrease of  $E\%$  with increasing  $uD$ : acceptor ( $uD:A$ ) ratio and  $uD$  levels, which is especially useful when acceptor data is not available. Furthermore, we have developed novel mathematical models that explain the decrease of  $E\%$  with increasing  $uD:A$  ratios. The model is based on the Förster theory of FRET and takes into account hard-core interactions between membrane components. We have also used these models to estimate the local density of labeled ligand-receptor complexes in the neighborhood of a typical donor-labeled ligand-receptor complex. In summary, our results have demonstrated the clustering of ligand-receptor complexes during protein sorting and transport in apical endocytic compartments. Our analysis of receptor distribution in membranes should be readily applicable to other examples of clustering—or lack thereof—of membrane-bound components.

## MATERIALS AND METHODS

### Culture of MDCK cells on filter inserts

MDCK cells stably transfected with pIgA-R were placed on top of an inverted Transwell Clear insert (Corning Costar, Cambridge, MA) to allow their direct visualization using an inverted microscope (Brown et al., 2000). These cells are grown for three days on filters in DMEM/10% FBS/Pen-Strep to achieve a fully polarized status (Barroso and Sztul, 1994).

### Internalization of fluorophore-labeled ligands

Polarized MDCK cells transfected with rabbit pIgA-R are washed with PBS, equilibrated with DMEM/HEPES/BSA at 17°C and internalized for 4 h at 17°C with pIgA-R pseudo-ligands ([Fab]<sub>2</sub> fragments of IgG antibodies raised against the extracellular domain of the rabbit pIgA-R) conjugated to Alexa488 (Molecular Probes, Eugene, OR) or Cy3 (Amersham Life Science, Pittsburgh, PA) from the apical and basolateral PM, respectively (Barroso and Sztul, 1994). In all, three different samples were used: the double-labeled specimen, containing apically internalized Alexa488-pIgA-R-ligand complexes (*donor*) and basolaterally internalized Cy3-pIgA-R-ligand complexes (*acceptor*), plus corresponding single-labeled donor or acceptor reference samples containing either Alexa488 or Cy3, respectively. Then, cells are washed with PBS and fixed with 4% paraformaldehyde/PBS. High concentrations of pIgA-R ligands (40–160 μg/ml) were used to minimize the presence of empty receptors. pIgA-R ligands were shown to be transported across the polarized MDCK cells in a manner similar to dIgA, the

physiological ligand of pIgA-R, as described in Barroso and Sztul (1994). At 17°C, delivery to the apical PM is blocked and both ligand-receptor complexes accumulate in apical endocytic compartments, located ~2–4  $\mu\text{m}$  below the apical PM (Hunziker et al., 1990; Barroso and Sztul, 1994) (Fig. 1).

## Data collection

We used SimplePCI software (Compix, Cranberry Township, PA) and a Nikon PCM 2000 laser scanning confocal microscope, equipped with a 60 $\times$  water immersion lens 1.2 NA, Argon (488 nm) and Green HeNe (543 nm) laser, emission filters 515/50 nm and 590 nm LP, respectively, to acquire images from all three types of specimen under the exact same conditions (PCM 1024  $\times$  1024 color, 2.3 $\times$  zoom, no processing). Data collection details are described in Elangovan et al. (2003). Cell height was checked (~15–20  $\mu\text{m}$ ) and images were collected at 3.5  $\mu\text{m}$  below the apical PM where apical endocytic compartments are located.

## Bleaching experiments

Double-labeled and single-labeled acceptor and donor samples were imaged under similar conditions to collect acceptor/donor excitation images at time '0'. For the *bleaching-the-donor* experiments, this is followed by 30 s of bleaching with the argon laser (donor excitation—both donor channel and acceptor channel fluorescence is collected simultaneously), switching to the acceptor excitation and taking a one-scan image. Another period of 30 s of argon laser bleaching is then performed until a total of 5 min of bleaching time has been accumulated. The *bleaching-the-acceptor* experiments were conducted as described previously (Jovin and Arndt-Jovin, 1989; Gadella and Jovin, 1995; Bastiaens and Jovin, 1996; Kenworthy and Edidin, 1998). After finding the right cellular location, the zoom is changed to 10 $\times$ , which results in the capture of only the centrally located region of interest (ROI). The HeNe laser is now allowed to scan continuously until the acceptor is bleached, which takes ~10 min. The zoom is changed back to 2.3 $\times$  and new one-scan images are taken separately with the HeNe (*acceptor*) and Argon (*donor*) lasers. Under acceptor excitation in the acceptor channel, the bleached “window” is clearly visible, allowing us to establish the pixel coordinates and the registration of different images, thus correcting any slippage. The donor fluorescence (donor excitation/donor channel) within this bleached window, before and after bleaching the acceptor corresponding to the quenched and *uD* fluorescence, forms the basis of calculation for the energy transfer.

## Postacquisition data generation

There are two contaminants in the FRET signal: donor cross-talk and acceptor bleedthrough. We are using a novel algorithm (Elangovan et al., 2003) which removes these contaminants pixel-by-pixel on the basis of matched fluorescence levels between the double-label specimen and a single-label reference specimen, using seven images: two single-label donor reference images (donor excitation/donor channel and acceptor channel; data not shown); two single-label acceptor reference images (donor and acceptor excitation, both in the acceptor channel; data not shown); and three double-label images (acceptor excitation/acceptor channel, and donor excitation/donor and acceptor channels; Fig. 2, A–C). The donor excitation/donor channel shows the quenched donor (*qD*) fluorescence (Fig. 2 B), whereas the acceptor excitation/acceptor channel indicates the acceptor fluorescence (Fig. 2 A). The donor excitation/acceptor channel corresponds to the uncorrected FRET (uFRET) image (Fig. 2 C), which is then algorithm-processed to generate the precision-FRET (PFRET) image (Fig. 2 D), showing the corrected energy transfer levels.

The pixel-by-pixel correction used to generate the PFRET image is actually based on the average value of narrow fluorescence ranges, for more

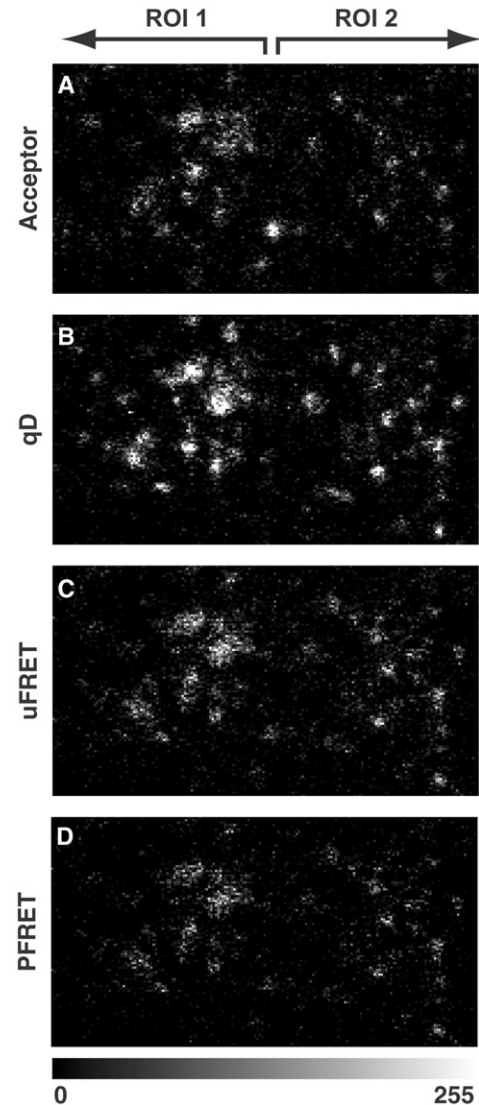


FIGURE 2 Imaging acceptor, *qD*, uFRET, and PFRET distributions of pIgA-R-ligand complexes in apical endocytic membranes. Double-labeled MDCK polarized cells, containing apically internalized Alexa488-pIgA-R-ligand complexes (donor) and basolaterally internalized Cy3-pIgA-R-ligand complexes (acceptor), were imaged by confocal microscopy at an *x-y* (*z*-section) focal plane ~3.5  $\mu\text{m}$  below the apical PM under the same imaging conditions. These images were modified in Adobe Photoshop at the same rate to a higher level of contrast for better visualization. Images shown (overall size, 16.2  $\mu\text{m}$   $\times$  8.7  $\mu\text{m}$ ) contain two ROIs of similar size (7.48  $\mu\text{m}$   $\times$  7.48  $\mu\text{m}$ ), each one containing a complete cell. (A) Acceptor excitation/acceptor channel shows acceptor fluorescence intensities. (B) Donor excitation/donor channel shows the *qD* fluorescence intensities. (C) Donor excitation/acceptor channel represents uFRET, which includes energy transfer levels plus the two contaminants in the FRET signal: donor cross-talk and acceptor bleed-through. (D) PFRET image. Image C was processed by our custom correction algorithm, which removes donor cross-talk and acceptor bleed-through. The resulting image represents the actual energy transfer levels.

efficient running of the correction algorithm (Elangovan et al., 2003). In our case, we chose the average of 12 fluorescence units, i.e., 0–12, 13–24, etc., continuing to the highest fluorescent units in the image. Using the average of even narrower ranges did not improve the sensitivity.

## Postacquisition data analysis

The single-number Förster-type energy transfer  $E$  is described as the ratio of energy transfer to the total sum of rates for all processes by which the excited donor can return to its ground state. Thus,  $E$  is based on the energy that is transferred from the donor to the acceptor and is dependent on the distance between donor and acceptor fluorophores and the geometry of binding of the donor/acceptor pair (Wouters et al., 2001; Lakowicz, 1999). In contrast, apparent  $E\%$  is not only dependent on  $E$ , but is also influenced by the concentrations of free and bound donor or acceptor molecules. By this definition, most references in the literature, including our measurements, fall into the category of apparent  $E\%$ , which, for brevity we will continue to call  $E\%$  in this article.

$E\%$  is an expression of the energy transfer as a percentage of  $uD$ , as described in Eq. 1. There are different methods to establish  $E\%$ , the most widely used being *bleaching-the-acceptor* (Bastiaens and Jovin, 1996; Wouters et al., 1998). To avoid the potentially negative results of photobleaching, several FRET correction methods have been developed based on ratiometric approaches (Bastiaens and Jovin, 1996; Gordon et al., 1998; Chamberlain et al., 2000; Xia and Liu, 2001; Zal et al., 2002). Here, we have pursued an alternative algorithm-based approach, which allows us to establish a  $uD$  value by adding the PFRET value—representing total energy transfer—to the quenched donor ( $qD$ ) fluorescence and thus to calculate  $E\%$ . This Eq. 1 corresponds to Eq. 7 on Elangovan et al. (2003), such as  $qD = I_{DA}$  and  $uD = I_D$ , i.e.,  $I_D = I_{DA} + \text{PFRET}$ :

$$E = 1 - [I_{DA}/I_{DA} + \text{PFRET}]. \quad (1)$$

As a first step, we visually select appropriate regions of interest (ROIs—usually one complete cell) from the uFRET image and note their pixel coordinates. These pixel locations are applied to the other images and fluorescence values are extracted. A custom-written analysis program selects pixels between 10 and 254 arbitrary units in the uFRET image. Eliminating values below 10 arbitrary units removes background noise, which we previously established to be on average eight arbitrary units (data not shown). By not considering pixels at 255 units (the maximum of the range) we eliminate saturated pixels. The selected uFRET pixel locations are transferred to the  $qD$  image (donor excitation/donor channel) and pixels containing saturated donor fluorescence are eliminated (this is a precaution to avoid a potentially misleading calculation of the  $uD$  value; in actuality, there are very few saturated donor pixels). This final pixel selection became the template for all calculations. Acceptor,  $qD$ , and PFRET values are averaged over each ROI. These average values based on the original pixel-by-pixel analysis are used to calculate  $uD$ ,  $uD:A$ , and  $E\%$  (Eq. 1). We then plot the relationship of  $E\%$  to actual acceptor and  $uD$  levels and  $uD:A$  ratio. It is very important to determine the actual  $uD:A$  ratios, since MDCK cells internalized with equal concentrations of donor- and acceptor-labeled pIgA-R ligands show significant variability in their ability to internalize and transport them to the apical region, as observed by FRET confocal microscopy. Internalization and transport variability between MDCK cells can be caused by different pIgA-R expression levels and rates of transcytosis.

As described above, we have used fluorescence intensity to assess local concentrations of donor- and acceptor-labeled proteins by confocal fluorescence microscopy of the selected ROIs in fixed cells. Such an analysis and the FRET correction technique assume a constant cellular environment, which is a reasonable assumption for fixed cells. A comparison between different ROIs is possible since the excitation efficiencies ( $\epsilon$ ), quantum yields of the fluorophore molecules, and the detection efficiencies, ( $Q$ ), are assumed constant throughout the experiments; i.e., in Eq. 9 of Elangovan et al. (2003),  $\Psi_{dd}$ ,  $\Psi_{aa}$ , and  $Q_d$  remain constant. This FRET-based assay has also been applied to live cells (Elangovan et al., 2003). In summary, we have increased the sensitivity of our algorithm-based FRET assay in two ways: 1) by using the actual  $uD$  and acceptor values to calculate actual  $uD:A$  ratio; and 2) by thresholding our results, so that we only use pixels for evaluation, which have participated in energy transfer based on the uFRET image.

## RESULTS

### FRET assay

Images showing a two-dimensional  $z$ -section (i.e., in the  $x$ - $y$  plane) at  $\sim 3.5 \mu\text{m}$  below the apical PM were collected from double-labeled (Fig. 2, *A–C*) and single-labeled (data not shown) ROIs and then processed by a correction algorithm method (Elangovan et al., 2003) to generate the PFRET image (Fig. 2 *D*), which shows the energy transfer levels. The acceptor (Fig. 2 *A*),  $qD$  (Fig. 2 *B*) and the PFRET (Fig. 2 *D*) images are then used to calculate the three experimental parameters: acceptor,  $uD$ , and  $E\%$  values (Figs. 3–4). Comparing Fig. 2, *C* and *D*, it is clearly visible where contamination has been removed by treating the uFRET image with the correction algorithm. Fig. 2, *A–D* images, contain two representative ROIs of similar size (ROI 1–2), each corresponding to one cell, which show the typical punctate pattern of apical endocytic membranes located at the level of the apical cytoplasm.

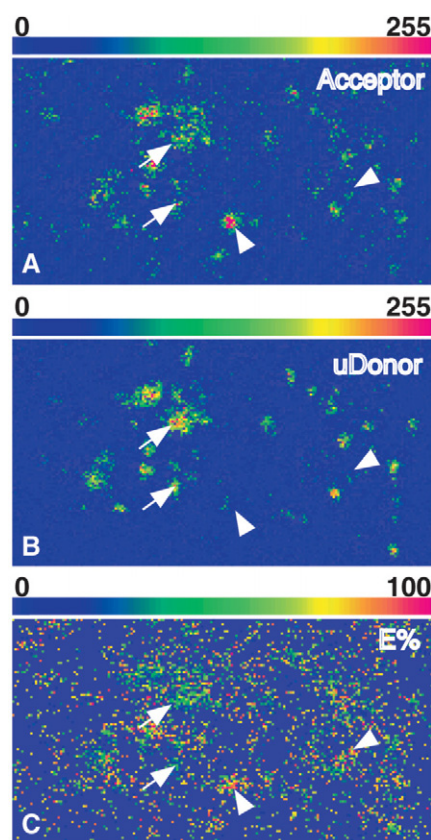


FIGURE 3 Pixel-by-pixel distribution of acceptor,  $uD$ , and  $E\%$  values in apical endocytic membranes. The two ROIs indicated in Fig. 2 were false-color-processed to show pixel-by-pixel distribution of acceptor (*A*),  $uD$  (*B*), and  $E\%$  (*C*) values. The image contains  $184 \times 99$  pixels (pixel size,  $88 \times 88$  nm) and each ROI contains  $85 \times 85$  pixels. Higher levels of  $uD$  correlate with lower  $E\%$  levels and vice-versa. Arrows show pixels with high  $uD$ /low  $E\%$ , whereas arrowheads indicate low  $uD$ /high  $E\%$ .

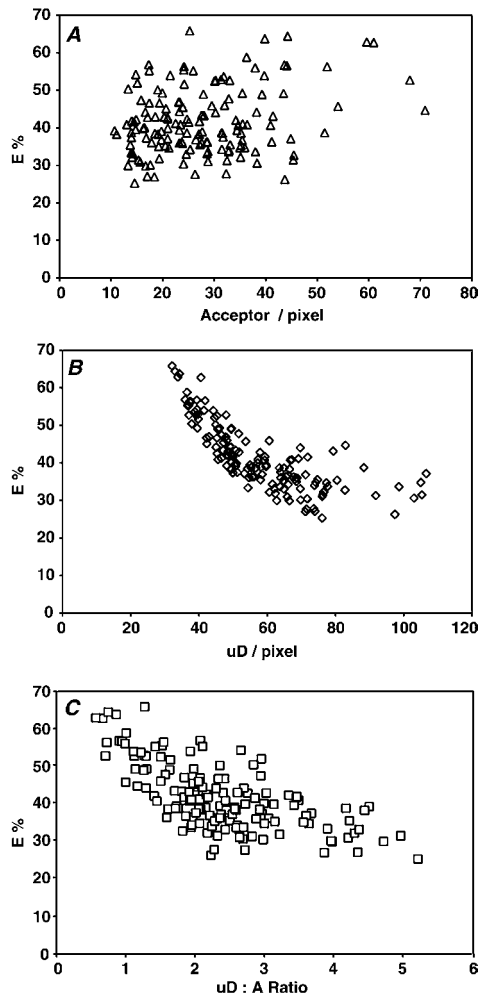


FIGURE 4  $E\%$  is largely independent of acceptor levels and decreases with increasing  $uD$  levels and  $uD:A$  ratios. 147 ROIs similar to those shown in Figs. 2–3 were assayed for acceptor and  $uD$  levels,  $uD:A$  ratios and  $E\%$ .  $E\%$  was plotted against acceptor levels (A, triangles),  $uD$  levels (B, diamonds), and  $uD:A$  ratios (C, squares).

### Pixel-by-pixel visualization of acceptor, $uD$ , and $E\%$ values

In Fig. 3, false-color images depicting the three experimental parameters that enter into our analysis of receptor cluster density are shown in a pixel-by-pixel manner for the two ROIs shown in Fig. 2. These false-color images represent the acceptor (Fig. 3 A),  $uD$  (Fig. 3 B), and  $E\%$  (Fig. 3 C) levels. Generally, the typical irregular and punctate endosomal pattern of the apical endocytic membranes is seen across all images. The  $uD:A$  ratio pixel information was used as a template to construct the  $E\%$  image, by selecting ratio values of  $>0$  and  $\leq 10$ , which had the effect of isolating pixels containing donor- and acceptor-labeled molecules in comparable  $uD:A$  ratios to those assayed in the ROI-based analysis (Fig. 4 C). A number of observations can be made concerning the  $E\%$  image presentation: there is a higher level of sensitivity apparent than in the other images, without

losing the overall endosomal morphology. Pixel locations with high  $uD$  levels show lower  $E\%$  values (Fig. 3, arrows), a phenomenon that is also clearly seen in the ROI-based analysis (Fig. 4 B). Conversely, pixel locations with low  $uD$  levels show high  $E\%$  values (Fig. 3, arrowheads). Also, individual and groups of 2–3 pixels are detected showing higher  $E\%$ , which could represent individual vesicles budding from, or on their way to dock onto, the endosomal membrane.

### Clustered distribution of plgA-R-ligand complexes in apical endocytic membranes

To determine whether ligand-receptor complexes are randomly distributed or clustered in apical endocytic membranes, we chose a large number of ROIs (147), each representing one complete cell, and a wide range of  $uD$  and acceptor values to create as broad a database as possible. We show that  $E\%$  is largely independent of acceptor levels (Fig. 4 A) and decreases with rising  $uD$  levels (Fig. 4 B), and  $uD:A$  ratio (Fig. 4 C). Correlation analysis substantiates these conclusions, with values of  $r = 0.27$ ,  $r = -0.76$ , and  $r = -0.66$ , respectively. These effects persist, if  $E\%$  is analyzed as a function of two variables (acceptor levels and  $uD:A$  ratio) simultaneously (data not shown). The linear relationship between acceptor and  $E\%$  levels is rather weak, as indicated by the low value of the slope,  $0.21 \pm 0.12$  (0.09–0.33 at a 95% confidence interval). To dissect this relationship between acceptor levels and  $E\%$ , we have divided the  $E\%$  data in 10 groups depending on acceptor levels (Table 1). ANOVA test on these groups yielded a  $p$ -value indicating significant evidence that the means are not all equal ( $p = 0.0134$ ). However, simply removing either the last two groups or the four datapoints with the highest acceptor levels results in a reduced value of  $p = 0.2454$ , indicating a lack of evidence of dependence (Table 1). This analysis strongly indicates that in our experimental system,  $E\%$  is largely independent of acceptor levels and does not decrease toward zero with decreasing acceptor levels.

TABLE 1 ANOVA (single factor) test for Fig. 4 A

Group	Acceptor Ranges	Count	Average ( $E\%$ )	Variance
1	10–14	17	38.46	49.09
2	15–19	27	40.14	71.10
3	20–24	26	42.14	46.78
4	25–29	22	40.18	70.30
5	30–34	21	41.46	64.71
6	35–39	16	43.67	105.93
7	40–44	9	45.61	146.48
8	45–49	2	32.10	0.84
9	50–54	3	46.92	78.27
10	$>55$	4	55.75	77.03
Treatments		$F$	$P$ -value	$F$ -crit
Groups 1–10		2.44	0.0134	1.95
Groups 1–9		1.31	0.2454	2.01



Positive controls included co-internalizing both differently labeled ligands from the same PM for 4 h at 17°C. As expected, FRET occurred at every stage of the transcytotic/endocytic pathways starting at the PM (data not shown). Single-labeled specimens serve as negative controls, where at the donor excitation wavelength, the acceptor channel image represents bleedthrough (data not shown).

To find out how our algorithm-based energy transfer efficiency results compare with the standard method of bleaching-the-acceptor, we conducted an experiment according to this method. Confirming our previous results, the bleaching-the-acceptor  $E\%$  results are also largely independent of acceptor fluorescence levels indicating a clustered distribution (Fig. 5 A).  $E\%$  values fall within the same ranges (20–40%), as the majority of ROIs do in experiments using the algorithm correction method (35–50%). As expected in a direct comparison between the two systems, standard deviation ranges (*error bars*) overlap (Fig. 5 B). Furthermore, correlation analysis between acceptor fluorescence and  $E\%$  for the algorithm method has a coefficient of  $r = 0.27$  and for the bleaching-the-acceptor  $r = -0.07$ , both indicating that the  $E\%$  is largely independent of acceptor levels.

### Donor-bleaching experiments show that not all donors are equally involved in FRET

Total  $uD$  levels entering into the computation of  $E\%$  include all donors, i.e., those that participate in FRET (FRET

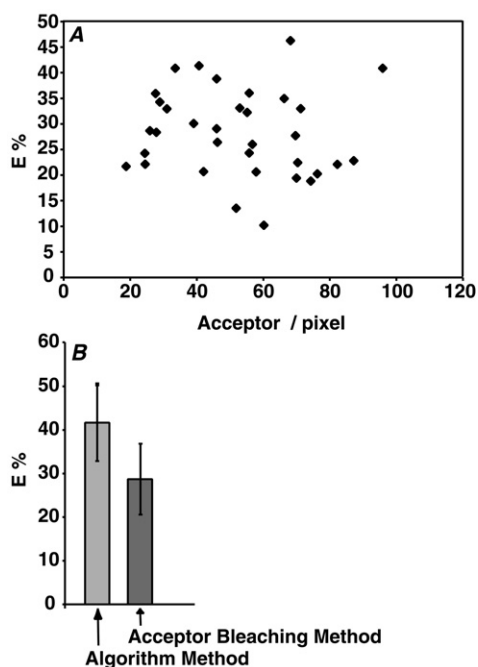


FIGURE 5  $E\%$  is independent of acceptor levels by the bleaching-the-acceptor technique. The standard method of bleaching-the-acceptor was used to validate our algorithm approach. (A)  $E\%$  was plotted vs. acceptor values. (B) The bleaching-the-acceptor results fall within the same range as those produced by our algorithm with overlapping standard deviations.

donors), and those which do not (non-FRET donors). Eq. 1 can therefore be restated as:

$$E\% = 100 \times PFRET / [uD(FRET) + uD(non-FRET)]. \quad (2)$$

To test for the presence of non-FRET and FRET donors, we have performed donor photobleaching experiments by exposing single donor- and double-labeled specimens to 10 consecutive 30-s periods of donor excitation laser and taking measurements after each bleaching period. Donor photobleaching discriminates between FRET and non-FRET donors because energy transfer constitutes an additional pathway for de-excitation, and FRET donors will spend less time in the excited state and therefore bleach less than non-FRET donors. We selected five ROIs with an average of  $\sim 1.5 uD:A$  ratio and corresponding  $E\% \sim 21\%$  at  $t = 0$  and plotted the normalized average  $uD$  levels versus cumulative donor bleaching time (Fig. 6 A).  $uD$  levels show a faster rate of bleaching in single-labeled donors, which only contain non-FRET donors, than in double-labeled samples; all double-labeled  $uD$  normalized datapoints are higher than the single-labeled  $uD$  with no overlap between their standard deviation ranges (Fig. 6 A). Performing a  $t$ -test for  $uD$  levels at each timepoint confirms the significance of the  $uD$  behaviors in 10 out of 10 normalized datapoints (Table 2). As shown in Fig. 6 B, exponential decay curves were fitted to the experimental data (Fig. 6 A), considering the following lifetimes for the donor molecule in the absence or presence of acceptor:  $\tau D_{\text{donor single-labeled}} = 142.25 \pm 19.9$  and  $\tau D_{\text{double-labeled}} = 190.05 \pm 11.9$ . The fit between the exponential decay curves and the experimental data is confirmed by the correlation coefficients of  $r = 0.979$  and  $r = 0.972$  for double-labeled and single-donor-labeled  $uD$  levels, respectively. Thus, these results clearly suggest the presence of FRET donors in the double-labeled samples, since their absence should result in identical rates of donor bleaching in double-labeled and donor single-labeled samples.

In Fig. 6 C, we have compared average normalized  $uD$  levels vs. average normalized  $E\%$  at cumulative donor bleaching timepoints for the ROIs analyzed in Fig. 6, A–B. After a period of 300 s of bleaching,  $E\%$  increases 1.5–2 $\times$  as  $uD$  levels decrease dramatically by >80%. ANOVA analysis shows a  $p$ -value = 0.000248, indicating a significant difference between  $E\%$  datapoints. Furthermore, a linear fit with a correlation efficiency of  $r = 0.991$  confirms the strong positive relationship between  $E\%$  and donor bleaching time. We attribute the increase of  $E\%$  with bleaching time in Fig. 6, A–B, to the presence of non-FRET donors being bleached ahead of FRET donors in double-labeled clusters.

To address the behavior of acceptor levels under donor photobleaching conditions, we collected acceptor channel images under acceptor excitation at each donor bleaching timepoints from acceptor single-labeled and double-labeled samples. Acceptor levels show a slower rate of bleaching at each timepoint than donor values, since acceptor molecules

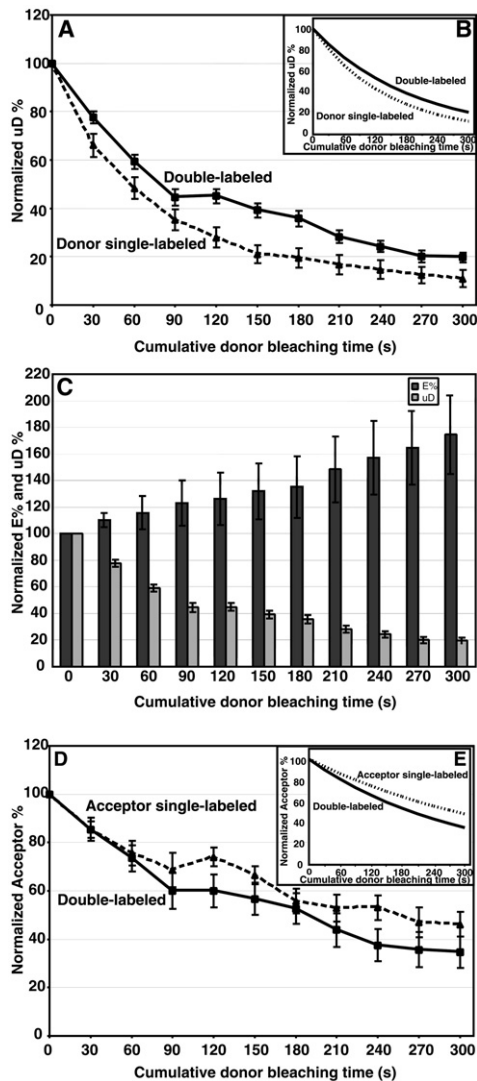


**FIGURE 6** Donor photobleaching shows the presence of FRET and non-FRET donors in double-labeled samples. Five ROIs of donor and acceptor single-labeled and double-labeled specimens were subjected to continuous donor excitation laser for periods of 30 s for a total of 5 min, with datapoints taken at each 30-s interval. (A) The normalized averages of  $uD$  levels in double-labeled (solid squares/solid line) and donor single-labeled samples (solid triangles/dotted line) plotted against the cumulative donor bleaching time (s). (B) Exponential decay curves fitted to the experimental data shown in A (double-labeled, solid line; donor single-labeled, dotted line). (C) The normalized  $uD$  and  $E\%$  levels over donor bleaching time. (D) The normalized averages of acceptor levels in double-labeled (solid squares/solid line) and acceptor single-labeled samples (solid triangles/dotted line) plotted against the cumulative donor bleaching time (s). (E) Exponential decay curves fitted to the experimental data shown in D (double-labeled, solid line; acceptor single-labeled, dotted line). As expected, donor molecules bleached faster in the donor single-labeled than in the double-label samples (A–B), while acceptor molecules bleached faster in the double-labeled than in the acceptor single-labeled samples (D–E). The decrease in  $uD$  levels by photobleaching leads to an increase in  $E\%$  (C) as non-FRET donors bleach faster;  $E\%$  increases 1.2–2 times, whereas  $uD$  decreases by >80%. Overall, these results indicate that non-FRET as well as FRET donors are present in the double-labeled specimens.

**TABLE 2**  $p$ -values for a two-tailed  $t$ -test analysis (assuming equal variances) for Fig. 6, A and D

Time(s)	uDonor*	Sig. <sup>†</sup>	Acceptor <sup>‡</sup>	Sig. <sup>†</sup>
30	0.0013	+	0.9910	–
60	0.0018	+	0.5438	–
90	0.0048	+	0.0991	–
120	6.64E-05	+	0.0043	+
150	2.35E-05	+	0.0225	+
180	9.56E-05	+	0.4233	–
210	0.0006	+	0.0517	–
240	0.0016	+	0.0032	–
270	0.0032	+	0.0287	–
300	0.0014	+	0.0137	–

\*Comparison of uDonor between double-labeled and donor single-labeled.

<sup>†</sup>Sig. (significance) columns: (+) indicates that the  $p$ -value is significant at the 95% level and (–) indicates that the  $p$ -value is not significant at the 95% level.

<sup>‡</sup>Comparison of acceptor between double-labeled and acceptor single-labeled.

are only partially excited by the donor laser wavelength, due to the spectral overlap between acceptor and donor fluorophores (Fig. 6 D). Acceptor fluorophores bleach faster in the presence of donor than in its absence, since, in the double-labeled samples, the acceptor will be excited to a greater level via FRET and as fluorescence increases, bleaching will also. As shown in Fig. 6 E, exponential decay curves were fitted to the experimental data (Fig. 6 D), considering the following lifetimes for the acceptor molecule in the absence or presence of donor:  $\tau A_{\text{acceptor single-labeled}} = 406.55 \pm 49.4$  and  $\tau A_{\text{double-labeled}} = 285.01 \pm 48.6$ . The fit between exponential decay curves and the experimental data is confirmed by the correlation coefficients values of  $r = 0.985$  and  $r = 0.972$  for double-labeled and single-acceptor labeled acceptor levels, respectively. A  $t$ -test for acceptor levels at each timepoint confirms the significance of the acceptor behaviors in seven out of 10 normalized datapoints (Table 2).

It has been shown before that donor photobleaching is an alternative way to measure FRET (Gadella and Jovin, 1995; Wouters et al., 1998; Schmid et al., 2001; Glauner et al., 1999). The donor photobleaching rate decreases proportionally to the reduction of the lifetime of the donor's excited state that is generated from the occurrence of a FRET event. Although this method to measure  $E\%$  does not apply to our biological situation, where donor-acceptor pairs are separated by variable distances, it results in an average  $E\%$  of ~25% (considering that  $E\% = 100 \times 1 - \tau D_{\text{donor single-labeled}} / \tau D_{\text{double-labeled}}$ ), which is comparable to the average  $E\%$  (~21%) determined by our algorithm-based method at  $t = 0$ .

### Mathematical models to describe large clusters of membrane proteins

To distinguish between clustered and random distributions of labeled ligand-receptor complexes and to investigate the mechanism of the negative dependence of  $E\%$  on  $uD:A$  ratio

and  $uD$  levels, we have introduced several mathematical models for the distribution of proteins in membranes, under a few simplifying geometric assumptions (see detailed description in the Appendix). For random distribution, we have compared our discretized random model with the random distribution model (Dewey and Hammes, 1980) (Fig. 7, A–B); for clustered distribution, we have compared our perfect cluster model with the dimer model (Kenworthy and Edidin, 1998) (Fig. 7, C–D). The four models express the predicted  $E\%$  as a function of several parameters, including the Förster distance  $R_0$ , the distance of closest possible approach  $R$ , and the surface densities of the acceptor and donor fluorophores (Fig. 7). In our experiments,  $R_0$  and  $R$  are known quantities, and the acceptor and  $uD$  levels determine the respective surface densities up to a proportionality constant, which is determined by the fraction of the membrane surface area within a pixel that is covered by labeled ligand-receptor complexes. Our experimental results contradict the predictions of the random distribution models in three ways:

1. No significant dependence of  $E\%$  on acceptor surface density. In both random distribution models,  $E\%$  increases with increasing acceptor surface density and decreases to zero if acceptor surface density is taken to zero (Fig. 7 A). In contrast, in both cluster distribution models,  $E\%$  is independent of acceptor surface density (Fig. 7 C). Our data shows a weak positive dependence of  $E\%$  on acceptor levels for Fig. 4 A but not for Fig. 5 A. Furthermore,  $E\%$  does not go to zero at low acceptor levels (Fig. 4 A and Fig. 5 A); rather, dependency of  $E\%$  on rising acceptor levels is more noticeable at higher acceptor levels.

2. Decrease of  $E\%$  with  $uD:A$  ratio. In both random distribution models,  $E\%$  does not depend on  $D:A$  ratio (Fig. 7 B). In both cluster distribution models,  $E\%$  decreases with increasing  $uD:A$  ratio (Fig. 7 D). This agrees well with our data (Fig. 4 C).
3. Random model predictions of density of ligand-receptor complexes in apical endocytic membranes. A datapoint close to the median of the distribution in Fig. 4 C is given by  $uD:A = 2.5$ ,  $E\% = 40\%$ . For a random distribution, an  $E\% \sim 40\%$  would correspond to an acceptor surface density of  $\sim 13\%$  (our model), and 20% (Dewey and Hammes, 1980; see also our Fig. 7 A). At a  $uD:A$  ratio of 2.5, this would correspond to a fraction between 45% (our model) and 70% (Dewey and Hammes, 1980) of the entire apical endocytic membrane surface covered by labeled ligand-receptor complexes. In view of the many functions performed by the apical endocytic compartments, one would expect the actual percentage of the surface to be much lower.

In summary, our experimental data cannot be reconciled with the predictions of the random distribution models. The qualitative behavior fits the predictions of the two clustered models.

### Cluster density estimate

In Fig. 8 A, the upper curve is the prediction of the perfect cluster model with  $s = 1$  (see Appendix) and the lower curve is the prediction of the Kenworthy-Edidin dimer model, considering the parameter  $\mathbf{E}\{dimer\}$  as an adjustable parameter (Zacharias et al., 2002). Since the experimental

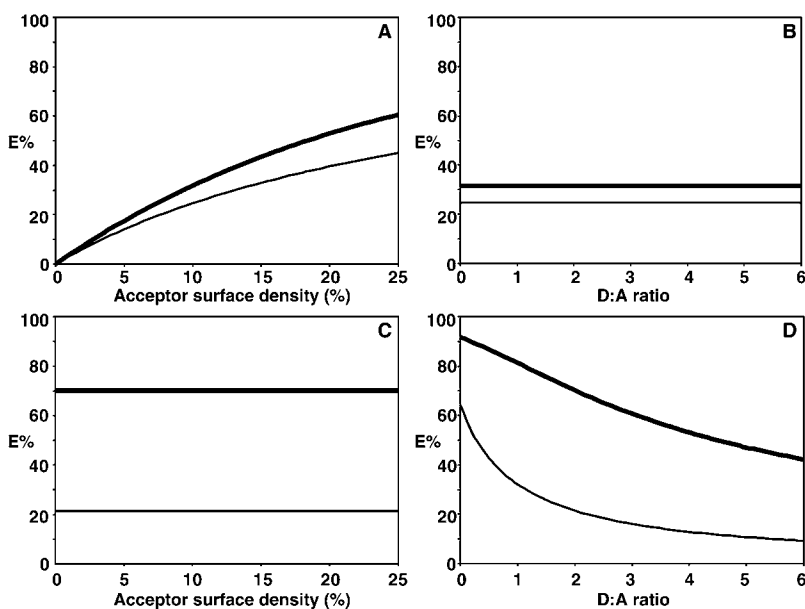
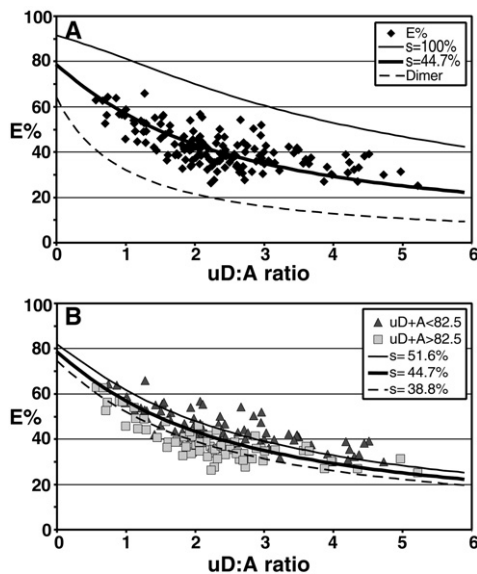


FIGURE 7  $E\%$  predictions of several models for different arrangement of labeled ligand-receptor complexes. (A–B)  $E\%$  predictions of two models for a random arrangement of labeled ligand-receptor complexes. The lower curves show the random distribution model (Dewey and Hammes, 1980) as given in Eq. A5, and the upper curves show our discretized random model, using Eq. A3, with  $s =$  fraction of membrane area covered by receptors. (A)  $E\%$  as a function of acceptor surface density (in %) for arbitrary  $D:A$  ratio. (B)  $E\%$  as a function of  $D:A$  ratio for a fixed acceptor surface density (shown for 10%). In both models,  $E\%$  is independent of  $D:A$  ratio, if acceptor surface density is kept fixed. It increases with acceptor surface density, and vanishes for small acceptor surface densities. (C–D)  $E\%$  predictions of two models for a clustered arrangement of labeled ligand-receptor complexes. The lower curves were computed with the dimer model (Kenworthy and Edidin, 1998), using  $E_{dimer}$  given by Eq. A4, and the upper curves were computed with our perfect cluster model, using Eq. A3 with  $s = 1$ . (C)  $E\%$  as a function of acceptor surface density (in %) for a fixed  $D:A$  ratio (shown for  $D:A = 2$ ). (D)  $E\%$  as a function of  $D:A$  ratio. In both models,  $E\%$  decreases with increasing  $D:A$  ratio, and is independent of acceptor surface density.





**FIGURE 8** Comparison of models for clustered distribution of ligand-receptor complexes with experimental data. (A) The bottom curve (*dotted line*) shows the dimer model (Kenworthy and Edidin, 1998),  $E_{\text{dimer}}$  given by Eq. A4. The top curve (*thin line*) shows the prediction of our perfect cluster model for an infinite, tightly packed cluster, as given in Eq. A3 with  $s = 1$ . The middle curve (*heavy line*) shows our fixed local density model, with the  $s$ -value adjusted to match the data. A least-squares fit results in an optimal value of  $s = 44.7\%$ , which provides a lower bound on the cluster density. See Fig. 10 for illustration of the role of  $s$  and  $D:A$  ratio. (B) The datapoints are the same as above, grouped by total fluorescence  $uD + A$ , as in  $uD + A > 82.5$  and  $uD + A < 82.5$ . The least-squares fit that best matches each group is given by  $s = 51.6\% \pm 5.4\%$  for  $uD + A < 82.5$  (*thin line*) and  $s = 38.8\% \pm 4.4\%$  for  $uD + A > 82.5$  (*dotted line*), suggesting the presence of distinct populations of ROIs with different average local density values depending on  $uD + A$ . In Fig. 9, C–D, a saturation model is proposed to address these results.

data fall between the predictions of the perfect cluster and the dimer models, we have matched our data to the fixed local density model (see Appendix). This model contains an adjustable parameter,  $s$ , which has the physical significance of the local density of labeled ligand-receptor complexes near a reference donor-labeled complex, and provides a lower bound on the cluster density. To obtain an estimate of cluster density, we performed a least-squares fit on the fixed local density model and found that the value of  $s$  that best matches our experimental data overall is given by  $s = 44.7\% \pm 6.5\%$  (Fig. 8 A).

To address the dependency of  $E\%$  on the total amount of labeled ligand-receptor complexes in apical endocytic membranes ( $uD + A$ ), we divided the data into two groups with  $uD + A < 82.5$  ( $n = 73$ ) and  $uD + A > 82.5$  ( $n = 74$ ) (Fig. 8 B). These two groups are statistically different, based on  $t$ -test analysis ( $p = 1.45E-06$ ). The least-squares fit that best matches each  $uD + A$  grouping is given by  $s = 51.6\% \pm 5.4\%$  for  $uD + A < 82.5$  and  $s = 38.8\% \pm 4.4\%$  for  $uD + A > 82.5$  (Fig. 8 B). Dividing the data into six groups of  $\sim 25$  datapoints, with increasing  $uD + A$ , shows a greater level of

heterogeneity in the local density  $s$ -values ( $s = 35.6\%–61.4\%$ ) while maintaining a strong negative dependence of  $s$  on  $uD + A$ . These results indicate the presence of distinct populations of ROIs with different average local density values depending on  $uD + A$ .

## DISCUSSION

### Establishing a clustered distribution for pIgA-R-ligand complexes in apical endocytic membranes

Using the FRET assay described here, we have demonstrated that pIgA-R-ligand complexes are distributed in a clustered manner in apical endocytic compartments of polarized MDCK cells. Two experimental parameters were used as indicators of clustering (Kenworthy and Edidin, 1998; Kenworthy et al., 2000; Pentcheva and Edidin, 2001): 1), independence of  $E\%$  from acceptor levels; and 2), negative dependence of  $E\%$  on  $uD:A$  ratio. Our ability to calculate actual  $uD:A$  ratios has allowed us to use the negative dependence of  $E\%$  on  $uD:A$  ratio to provide positive evidence of clustering of ligand-receptor complexes. Furthermore, our results also indicate that  $E\%$  is largely independent of acceptor levels. The weak positive dependence of  $E\%$  on acceptor levels seen in our FRET assay may be attributed to decreasing  $uD:A$  ratio with increasing acceptor levels.

The decrease of  $E\%$  with increasing  $uD:A$  ratio is a useful criterion to distinguish clustered from random distributions when acceptor and donor levels are not easily modulated, as for example in our ligand-receptor experiments and in other experiments in which donor and/or acceptor are overexpressed by transient transfection. When acceptor data is not available and/or quantitated, a negative dependence of  $E\%$  on  $uD$  levels can be used as a secondary indicator of a clustered distribution.

The Kenworthy-Edidin dimer model has been an important tool for understanding the effect of clustered distributions of labeled proteins on FRET. However, the reliance on dimers limits the applicability of the model to low densities of labeled ligands and small clusters. To address higher densities and extended clusters, we have developed new models for  $E\%$  in clustered distributions of membrane-bound components (see Appendix). Our models take into account that no two membrane components can occupy the same space; i.e., there is a ‘hard-core’ interaction between all components.

Addressing the hard-core interactions between membrane-bound components is a significant correction to existing models. It justifies the use of the dependence of  $E\%$  on the  $uD:A$  ratio as an indicator for a clustered distribution of membrane-bound components. In a random distribution of membrane-bound components,  $uD:A$  ratio is irrelevant, since donor-donor interactions are less likely to occur (Kenworthy and Edidin, 1998; Kenworthy et al., 2000; Pentcheva and Edidin, 2001). In a clustered distribution, hard-core in-

teractions can prevent some donor-labeled molecules from being in FRET distance from an acceptor-labeled molecule. We call this effect *geometric exclusion*. There are three possible ways for a donor-labeled ligand-receptor complex to be geometrically/spatially prevented from transferring energy to an acceptor-labeled complex in a clustered situation: 1), by another donor-labeled complex; 2), by an unlabeled ligand-receptor complex; or 3), by an unknown membrane component. Since we have saturated the ligands with excess dye during the conjugation phase and have used high labeled ligand concentration levels during internalization, we expect a reduced number of unlabeled ligand-receptor complexes or free/empty receptors to be present in apical endocytic membranes. If  $uD:A$  ratio is increased, geometric exclusion due to donor-labeled complexes plays a larger role, leading to a decrease in  $E\%$ . In our models, we have neglected donor-donor competition events that may also contribute to the decline of  $E\%$  with increasing  $uD:A$  ratio, since donors involved in donor-donor competition should be able to alternately transfer energy to the closest acceptor during the relatively long laser dwell time.

Geometric exclusion should result in the existence of two populations of donor-labeled ligand-receptor complexes: one that participates in energy transfer (FRET donors) and another that is prevented from participating in energy transfer by the presence of other molecules (non-FRET donors). The coexistence of FRET donors and non-FRET donors was validated by donor bleaching experiments, in which  $E\%$  increases markedly with donor bleaching time. This increase can be understood qualitatively from the well-known fact that non-FRET donors bleach at a faster exponential rate than FRET donors, since the former spend more time in the excited state, while the latter has an additional path for de-excitation. Considering Eq. 2, if both FRET and non-FRET donors are present in a sample, then  $E\%$  will rise significantly under bleaching. If all donor fluorophores were equally involved in FRET, the resulting reduction of donor-donor competition would lead to only a small increase in  $E\%$ . These data confirm the existence of donors not involved in FRET under our experimental conditions.

### Quantitative analysis of local cluster density

The Kenworthy and Edidin model describes the distribution of dimers at low density, whereas our perfect cluster model describes the other extreme of a large and dense cluster, and it is therefore not surprising that the actual experimental results fall between the two models. To obtain an estimate of cluster density, we used the fixed local density model, using  $s$  as an adjustable parameter (see Appendix). The value of  $s$  that best fits a given data set provides an estimate of the local density of labeled ligand-receptor complexes near a typical donor-labeled ligand. In a large cluster,  $s$  coincides with the cluster density (see Appendix). In a random distribution,  $s$  signifies the density of ligand-receptor complexes, as a

fraction of the membrane surface area. In a mixed situation,  $s$  is a weighted average of the two situations described above, and thus gives a lower bound on cluster density. We have shown that the cluster model with density  $s = 44.7\%$  best fits our data. This value of  $s$  implies that on average, a donor-labeled ligand-receptor complex will have 2.5–3 labeled complexes in its immediate neighborhood. It also implies that cluster density is no lower than 44.7%. Our analysis may underestimate  $s$  because it neglects two effects that could reduce  $E\%$ : finite cluster size and donor-donor competition.

The parameter  $E\{dimer\}$  in the Kenworthy-Edidin dimer model could similarly be treated as an adjustable parameter (Zacharias et al., 2002). The parameter has the physical significance of describing the probability of FRET occurring in a dimer consisting of two differently labeled ligands. A least-squares fit yields that the parameter value that best matches the data in Fig. 8 is  $E_{dimer} = 124.3\%$  (data not shown), which is clearly inconsistent with the interpretation of the parameter as a probability (see Appendix, dimer model). Unlike the fixed local density model, the dimer model does not allow estimations of cluster density.

It is important to notice that our FRET analysis does not allow us to estimate the actual cluster size. This is a principal limitation of FRET analysis, since  $E\%$  depends only on the number of donor-acceptor pairs that are within the Förster distance and not on the global arrangement of membrane components. Thus, FRET data contains only information about the cluster density in the neighborhood of a typical donor-labeled protein, but does not differentiate between a large, loosely packed cluster and a collection of oligomers, if they share similar  $s$ -values. Nevertheless, the ability to determine the local density of clusters of membrane-bound components provides insights into the distribution of proteins in membranes with significant biological implications (see below).

### Biological implications

Membrane proteins can be organized in clusters or distributed randomly—or show a mixture of these two situations. Assembly of membrane components into patches, microdomains, rafts, or clusters before transport seems to be a ubiquitous sorting mechanism employed by the cell for many different pathways and has been described by many authors (Pentcheva and Edidin, 2001; Galbiati et al., 2001; Ikonen, 2001; Kobayashi et al., 2001; Maier et al., 2001; Mukherjee and Maxfield, 2000; Woodman, 2000). However, the presence of microdomains in endosomal membranes is still controversial (Hansen et al., 1999; Kobayashi et al., 2001; Sarnataro et al., 2000), possibly because of the transient nature and size of these domains (Tang and Edidin, 2001; Brown and Jacobson, 2001). We define *microdomains* as a concentration of clustered molecules within a membrane plane. The formation of transient membrane microdomains is thought to be an important element of this trafficking process

(Galbiati et al., 2001; Ikonen, 2001; Kobayashi et al., 2001; Maier et al., 2001; Mukherjee and Maxfield, 2000; Woodman, 2000). We postulate that protein clustering is essential for the formation of membrane microdomains, which most likely involves other processes and effectors such as coat-proteins, the cytoskeleton, signal sequences, and specific affinities between proteins and membrane lipids (Mukherjee and Maxfield, 2000; Woodman, 2000; Simons and Ikonen, 1997; Verkade et al., 2000; Sonnichsen et al., 2000).

Our findings showing that ligand-receptor complexes are distributed in a clustered manner in apical endocytic membranes strongly suggest that the clustering of membrane components occurs throughout protein sorting and transport in polarized cells. The dependence of local cluster density parameter  $s$  on the total concentration of labeled molecules gives some insight into this clustering mechanism. If ligand-receptor complexes behaved in a straightforward like-associates-with-like manner, then we would expect cluster density to increase with higher levels of labeled ligand-receptor complexes (Fig. 9 A). However, we clearly observe that  $s$  decreases with increasing levels of labeled ligand-receptor complexes, suggesting that clustering may occur only at a limited number of discrete locations on the membrane and/or require a specific protein that can be saturated (Fig. 9 B). Unorganized donor- and acceptor-labeled ligand-receptor complexes, outside the saturated clusters,

have the effect of lowering the overall density (Fig. 9 D). Recently, different density levels have also been suggested for T-cell receptor-CD4 clusters (Zal et al., 2002). Our density analysis should be particularly valuable to address receptor cluster density in different experimental systems. In summary, we propose that differences in energy transfer between ROIs or even between pixels within an ROI represent different local densities of acceptor- and donor-labeled molecules within clusters. Such different densities may reflect progressive sorting stages of ligand-receptor complexes within apical endocytic membranes that could be involved in the ability of proteins to be specifically incorporated into transport vesicles budding off from apical endocytic compartments.

## APPENDIX

### Models for FRET efficiency in clustered and unclustered arrangements of labeled membrane components

Models for small oligomers, and in particular dimers, have been used to analyze FRET efficiency ( $E\%$ ) as a function of both acceptor surface density and donor:acceptor ratio. The predictions of dimer models are expected to be valid so long as acceptor and donor surface densities are low, and typical cluster sizes are small. We present here a new clustering model, which is tailored to large clusters or high acceptor and donor surface densities.

### Physical assumptions

Consider a single excited donor molecule in the presence of a number, ( $k$ ), of acceptor molecules located at distances  $r_1, \dots, r_k$  from the donor. The Förster model predicts that the probability of the excited donor to return to the ground state via FRET is given by

$$E = 1 - \left\{ 1 + \sum_{i=1}^k (R_0/r_i)^6 \right\}^{-1}, \quad (\text{A1})$$

where  $R_0$  is the Förster distance, a physical constant of the involved donor and acceptor fluorophores. By definition, the probability that an excited donor molecule returns to the ground state through FRET is 50%, if a single acceptor molecule is located at a distance  $R_0$ . To analyze the dependence of FRET on experimental parameters, we combine Eq. A1 with a model for the geometric distribution of fluorophores.

Our experimental system assays the distribution of polymeric IgA-receptor (pIgA-R)-ligand complexes in endocytic membranes. The relevant parameter values are as follows:

*Förster distance.*  $R_0 = 67.5 \text{ \AA}$ .

*Protein shape and size.* The acceptor and donor fluorophores are attached to identical pseudo-ligands of pIgA-R, which are internalized from opposite membranes. The pIgA-R ligands occupy a cylindrical space with a circular cross section of diameter  $R = 80 \text{ \AA}$ .

*Receptor occupancy.* In our experimental approach, we attempt to saturate the receptors with increasing amounts of pIgA-R ligands to minimize the number of empty receptors.

*Number of fluorophores.* An average of five fluorophores per pIgA-R ligand, as indicated by the manufacturer. Experimentally, we saturate with fluorophores and hence assume that five binding sites are occupied with fluorophores and that the number of unlabeled ligands is low.

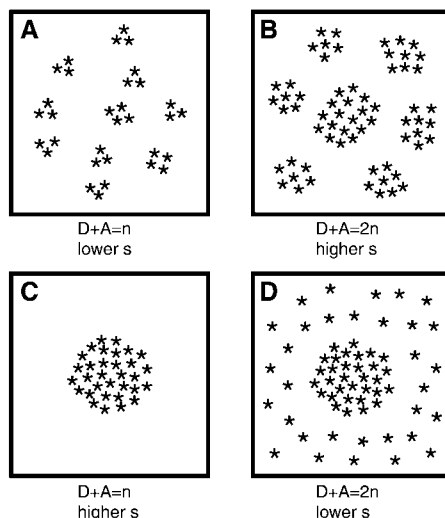


**FIGURE 9** Models for clustering mechanisms. (A–B) A simple *like-associates-with-like* model would suggest that increasing amounts of labeled ligand-receptor complexes ( $D + A$ ) results in increasing local cluster density. (C–D) A saturation-cluster model explains the negative dependence of local cluster density on increasing  $D + A$ . Left to right shows a doubling of the total number of donor and acceptor molecules ( $D + A$ ), i.e.,  $n$  to  $2n$ . The value of  $s$  indicates an estimation of the local cluster density as described in Fig. 8. In D, unorganized donor and acceptor molecules, outside the saturated cluster, have the effect of lowering the overall density. Each square represents a pixel area, and asterisks indicate the distribution of membrane-bound ligand-receptor complexes.

### The geometric model

We model the membrane as a two-dimensional surface, and we visualize the proteins of interest as disks in a plane directly above the membrane. The possible locations of proteins are discretized by covering the surface with disks in tight packing, so that each disk has six nearest neighbors (see Fig. 10). Each disk is either occupied by *A* or *D* (representing an acceptor- or donor-labeled ligand-receptor complex), or vacant (representing an unknown protein or absence of protein).

Suppose that a given reference disk is labeled by *D*. We assume that each of the neighboring disks is occupied by *A* with probability  $s_A$ , independently of all other disks, and correspondingly for *D* and vacant. Thus, we model the distribution of the number *N* of *A*-occupied neighbors of a given disk as a  $(6, s_A)$ -binomial random variable. We refer to  $s_A$  as the local density of *A*-labeled ligand-receptor complexes near the reference donor disk. We correspondingly define the local density  $s_D$  of *D*-labeled ligand-receptor complexes, and denote by  $s = s_A + s_D$  the total local density of ligand-receptor complexes. Then,  $s_A = s/(1 + D:A)$ . We distinguish two extreme situations:

*Discretized random model.* Here, the neighboring disks can be either occupied or vacant, and  $s$  = fraction of membrane area covered by ligand-receptor complexes.

*Perfect cluster model.* All disks in the neighborhood of a given donor are occupied by ligand-receptor complexes, i.e.,  $s = 1$ , describing a large and tightly packed cluster (Fig. 10, *A–B*).

The local density  $s$  of ligand-receptor complexes can also be treated as an adjustable parameter:

*Fixed local density model.* Disks in the neighborhood of any given disk are occupied by ligand-receptor complexes with probability  $s$ ,  $0 < s < 1$  (Fig. 10, *C–D*).

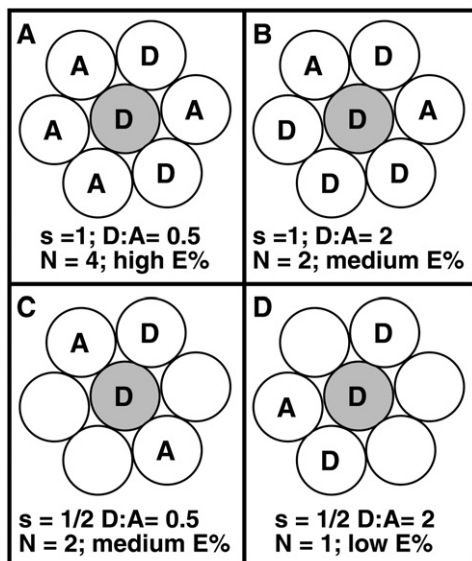


FIGURE 10 An illustration for the dependence of  $E\%$  on  $D:A$  ratio and the local density parameter  $s$ . The shaded circle represents a donor-labeled reference disk. Solid circles marked *A* or *D* represent acceptor-labeled or donor-labeled ligand-receptor complexes, and unfilled circles represent unknown proteins or absence of protein. (*A–B*) Perfect cluster model, Eq. A3 with  $s = 1$ , and  $D:A = 0.5$  (*A*) and  $D:A = 2$  (*B*), respectively. (*C–D*) The fixed local density model, Eq. A3 with  $s = 1/2$ , and  $D:A = 0.5$  (*C*), and  $D:A = 2$  (*D*), respectively.  $E\%$  decreases with increasing  $D:A$  ratio (*left to right*) and decreasing local density  $s$  (*top to bottom*), since fewer acceptors are available to the reference donor.

### Computation of $E\%$ in the model

To simplify computations, we replace the actual locations of the fluorophores in each disk by the average location at the center of the disk. Similarly, we replace the actual orientation of the fluorophores by an average over all possible orientations, corresponding to  $\kappa^2 = 2/3$  (Lakowicz, 1999). Since  $R > R_0$ , the contribution of all but adjacent disks to the right-hand side of Eq. A1 can be neglected. If  $N$  of the six neighbors of a *D*-occupied reference disk are occupied by *A*, then each donor fluorophore in the reference disk interacts with  $5N$  acceptor fluorophores whose average distance is approximately  $R$ . By Eq. A1 (with  $k = 5N$  and  $r_i = R$  for  $i = 1, \dots, k$ ), it contributes

$$E \approx 1 - \{1 + 5N(R_0/R)^6\}^{-1} \quad (\text{A2})$$

to the FRET signal. The factor 5 accounts for the number of fluorophores per labeled ligand (see Number of Fluorophores, in this section). We treat  $E$  and  $N$  as random variables, and compute the apparent  $E\%$  as an expected value,

$$E\% \approx \langle 1 - \{1 + 5N(R_0/R)^6\}^{-1} \rangle, \quad (\text{A3})$$

with respect to the  $(6, s_A)$ -binomial distribution. We assume that  $s_A = s/(1 + D:A)$ .

### Related models

For comparison, we also consider the following models:

*Dimer model* (Kenworthy and Edidin, 1998; cf. their Eq. A4). The apparent FRET efficiency in dimers is given by  $E\% = E_{\text{dimer}} A/(A + D)$ , where  $E_{\text{dimer}}$  is the FRET efficiency in a dimer consisting of two differently labeled pseudo-ligands. Using Eq. A2 with  $N = 1$  we estimate

$$E_{\text{dimer}} = 1 - \{1 + 5(R_0/R)^6\}^{-1} \approx 0.64. \quad (\text{A4})$$

Alternately,  $E_{\text{dimer}}$  could be determined experimentally, or used as an adjustable parameter (Zacharias et al., 2002).

*Random distribution model* (Dewey and Hammes, 1980; cf. their Eq. 22).

The first in a sequence of rational approximations is given by

$$E\%_{\text{random}} = 1 - \left[ \frac{5\pi}{\sqrt{3}} S_A \left( \frac{R_0}{R} \right)^6 \right]^{-1}, \quad (\text{A5})$$

where  $s_A$  is the fraction of the membrane area covered by acceptor-labeled ligand-receptor complexes.

In each case, the factor 5 accounts for the five fluorophores per labeled ligand.

The predictions of the four models are shown in Fig. 8.

We thank Sarah Smith for her assistance with the experiments and data analysis; Jeff Larson from Nikon for his help with confocal microscopy; Kathy Gerber, Information Technology and Communication, University of Virginia, for her help with scientific computing; Dr. G. Cox, University of Sydney, Australia, and Dr. J. Demas, Dept. of Chemistry, University of Virginia, for their helpful comments concerning the donor photobleaching experiments; Dr. D. Lake, Dept. of Mathematics, University of Virginia, for his help with the statistical analysis; Dr. J. Casanova, Dept. of Cell Biology, University of Virginia Medical School, and Dr. P. Bastiaens, European Molecular Biology Laboratory, Heidelberg, Germany, for their helpful comments. We also thank the members of the Keck Center for Cellular Imaging, Dr. L. Davidson, Dept. of Biology, University of Virginia, and the members of the laboratories of Dr. M. Barroso, Dr. G. Bloom, Dr. D. Shafer, and Dr. K. Kozminski, Dept. of Biology, University of Virginia, for helpful discussions.

## REFERENCES

- Apodaca, G., L. A. Katz, and K. E. Mostov. 1994. Receptor-mediated transcytosis of IgA in MDCK cells is via apical recycling endosomes. *J. Cell Biol.* 125:67–86.
- Barroso, M., and E. S. Sztul. 1994. Basolateral to apical transcytosis in polarized cells is indirect and involves BFA and trimeric G protein sensitive passage through the apical endosome. *J. Cell Biol.* 124:83–100.
- Bastiaens, P. I., and T. M. Jovin. 1996. Microspectroscopic imaging tracks the intracellular processing of a signal transduction protein: fluorescently labeled protein kinase C beta I. *Proc. Natl. Acad. Sci. USA.* 93:8407–8412.
- Brown, D. A., and K. Jacobson. 2001. Microdomains, lipid rafts and caveolae. *Traffic.* 2:668–672.
- Brown, P. S., E. Wang, B. Aroeti, S. J. Chapin, K. E. Mostov, and K. W. Dunn. 2000. Definition of distinct compartments in polarized Madin-Darby canine kidney (MDCK) cells for membrane-volume sorting, polarized sorting and apical recycling. *Traffic.* 1:124–140.
- Chamberlain, C. E., V. S. Kraynov, and K. M. Hahn. 2000. Imaging spatiotemporal dynamics of Rac activation in vivo with FLAIR. *Methods Enzymol.* 325:389–400.
- Day, R. N., A. Periasamy, and F. Schaufele. 2001. Fluorescence resonance energy transfer microscopy of localized protein interactions in the living cell nucleus. *Methods.* 25:4–18.
- Dewey, T. G., and G. G. Hammes. 1980. Calculation of fluorescence resonance energy transfer on surfaces. *Biophys. J.* 32:1023–1035.
- Elangovan, M., H. Wallrabe, R. N. Day, M. Barroso, and A. Periasamy. 2003. Characterization of one- and two-photon fluorescence resonance energy transfer microscopy. *Methods.* 29:58–73.
- Gadella, T. W., Jr., and T. M. Jovin. 1995. Oligomerization of epidermal growth factor receptors on A431 cells studied by time-resolved fluorescence imaging microscopy. A stereochemical model for tyrosine kinase receptor activation. *J. Cell Biol.* 129:1543–1558.
- Galbiati, F., B. Razani, and M. P. Lisanti. 2001. Emerging themes in lipid rafts and caveolae. *Cell.* 106:403–411.
- Gibson, A., C. E. Futter, S. Maxwell, E. H. Allchin, M. Shipman, J. P. Kraehenbuhl, D. Domingo, G. Odorizzi, I. S. Trowbridge, and C. R. Hopkins. 1998. Sorting mechanisms regulating membrane protein traffic in the apical transcytotic pathway of polarized MDCK cells. *J. Cell Biol.* 143:81–94.
- Glauner, K. S., L. M. Mannuzzo, C. S. Gandhi, and E. Y. Isacoff. 1999. Spectroscopic mapping of voltage sensor movement in the Shaker potassium channel. *Nature.* 402:813–817.
- Gordon, G. W., G. Berry, X. H. Liang, B. Levine, and B. Herman. 1998. Quantitative fluorescence resonance energy transfer measurements using fluorescence microscopy. *Biophys. J.* 74:2702–2713.
- Hansen, G. H., L. L. Niels-Christiansen, L. Immerdal, W. Hunziker, A. J. Kenny, and E. M. Danielsen. 1999. Transcytosis of immunoglobulin A in the mouse enterocyte occurs through glycolipid raft- and rab17-containing compartments. *Gastroenterology.* 116:610–622.
- Hansen, S. H., and J. E. Casanova. 1994. Gs alpha stimulates transcytosis and apical secretion in MDCK cells through cAMP and protein kinase A. *J. Cell Biol.* 126:677–687.
- Hunziker, W., P. Male, and I. Mellman. 1990. Differential microtubule requirements for transcytosis in MDCK cells. *EMBO J.* 9:3515–3525.
- Huttner, W. B., and J. Zimmerberg. 2001. Implications of lipid microdomains for membrane curvature, budding and fission. *Curr. Opin. Cell Biol.* 13:478–484.
- Ikonen, E. 2001. Roles of lipid rafts in membrane transport. *Curr. Opin. Cell Biol.* 13:470–477.
- Jovin, T. M., and D. J. Arndt-Jovin. 1989. FRET microscopy: digital imaging of fluorescence resonance energy transfer. Applications in cell biology. *In Cell Structure and Function by Microspectrofluorometry.* Academic Press, Orlando, FL.
- Kenworthy, A. K. 2001. Imaging protein-protein interactions using fluorescence resonance energy transfer microscopy. *Methods.* 24:289–296.
- Kenworthy, A. K., N. Petranova, and M. Edidin. 2000. High-resolution FRET microscopy of cholera toxin B-subunit and GPI-anchored proteins in cell plasma membranes. *Mol. Biol. Cell.* 11:1645–1655.
- Kenworthy, A. K., and M. Edidin. 1998. Distribution of a glycosylphosphatidylinositol-anchored protein at the apical surface of MDCK cells examined at a resolution of 100 Å using imaging fluorescence resonance energy transfer. *J. Cell Biol.* 142:69–84.
- Kobayashi, T., A. Yamaji-Hasegawa, and E. Kiyokawa. 2001. Lipid domains in the endocytic pathway. *Semin. Cell Dev. Biol.* 12:173–182.
- Lakowicz, J. R. 1999. Principles of Fluorescence Spectroscopy, 2nd Ed. Kluwer Academic/Plenum Publishers, New York.
- Leung, S. M., W. G. Ruiz, and G. Apodaca. 2000. Sorting of membrane and fluid at the apical pole of polarized Madin-Darby canine kidney cells. *Mol. Biol. Cell.* 11:2131–2150.
- Maier, O., T. A. Slimane, and D. Hoekstra. 2001. Membrane domains and polarized trafficking of sphingolipids. *Semin. Cell Dev. Biol.* 12:149–161.
- Mukherjee, S., and F. R. Maxfield. 2000. Role of membrane organization and membrane domains in endocytic lipid trafficking. *Traffic.* 1:203–211.
- Pentcheva, T., and M. Edidin. 2001. Clustering of peptide-loaded MHC class I molecules for endoplasmic reticulum export imaged by fluorescence resonance energy transfer. *J. Immunol.* 166:6625–6632.
- Periasamy, A., and R. N. Day. 1999. Methods in Cell Biology, Vol. 58, Ch. 18. Academic Press, San Diego.
- Samataro, D., L. Nitsch, W. Hunziker, and C. Zurzolo. 2000. Detergent insoluble microdomains are not involved in transcytosis of polymeric Ig receptor in FRT and MDCK cells. *Traffic.* 1:794–802.
- Schmid, J. A., P. Scholze, O. Kudlacek, M. Freissmuth, E. A. Singer, and H. H. Sitte. 2001. Oligomerization of the human serotonin transporter and of the rat GABA transporter 1 visualized by fluorescence resonance energy transfer microscopy in living cells. *J. Biol. Chem.* 276:3805–3810.
- Simons, K., and E. Ikonen. 1997. Functional rafts in cell membranes. *Nature.* 387:569–572.
- Sonnichsen, B., S. De Renzis, E. Nielsen, J. Rietdorf, and M. Zerial. 2000. Distinct membrane domains on endosomes in the recycling pathway visualized by multicolor imaging of Rab4, Rab5, and Rab11. *J. Cell Biol.* 149:901–914.
- Tang, Q., and M. Edidin. 2001. Vesicle trafficking and cell surface membrane patchiness. *Biophys. J.* 81:196–203.
- Van Ijzendoorn, S. C., O. Maier, J. M. Van Der Wouden, and D. Hoekstra. 2000. The subapical compartment and its role in intracellular trafficking and cell polarity. *J. Cell. Physiol.* 184:151–160.
- Verkade, P., T. Harder, F. Lafont, and K. Simons. 2000. Induction of caveolae in the apical plasma membrane of Madin-Darby canine kidney cells. *J. Cell Biol.* 148:727–739.
- Winckler, B., and I. Mellman. 1999. Neuronal polarity: controlling the sorting and diffusion of membrane components. *Neuron.* 23:637–640.
- Woodman, P. G. 2000. Biogenesis of the sorting endosome: the role of Rab5. *Traffic.* 1:695–701.
- Wouters, F. S., P. I. Bastiaens, K. W. Wirtz, and T. M. Jovin. 1998. FRET microscopy demonstrates molecular association of non-specific lipid transfer protein (nsL-TP) with fatty acid oxidation enzymes in peroxisomes. *EMBO J.* 17:7179–7189.
- Wouters, F. S., P. J. Verveer, and P. I. Bastiaens. 2001. Imaging biochemistry inside cells. *Trends Cell Biol.* 11:203–211.
- Wu, P., and L. Brand. 1994. Resonance energy transfer: methods and applications. *Anal. Biochem.* 218:1–13.
- Xia, Z., and Y. Liu. 2001. Reliable and global measurements of fluorescence resonance energy transfer using fluorescence microscopes. *Biophys. J.* 81:2395–2402.
- Zacharias, D. A., J. D. Violin, A. C. Newton, and R. Y. Tsien. 2002. Partitioning of lipid-modified monomeric GFPs into membrane microdomains of live cells. *Science.* 296:913–916.
- Zal, T., A. Zal, and N. R. J. Gascoigne. 2002. Inhibition of T-cell receptor-coreceptor interactions by antagonist ligands visualized by live FRET imaging of the T-hybridoma immunological synapse. *Immunity.* 16:521–534.